Monthly Notices of the ROYAL ASTRONOMICAL SOCIETY

MNRAS **468,** 3798–3812 (2017) doi:10.1093/mnras/stx683
Advance Access publication 2017 March 22

The late-time light curve of the Type Ia supernova SN 2011fe

G. Dimitriadis,[1⋆] M. Sullivan,[1] W. Kerzendorf,[2] A. J. Ruiter,[3,4] I. R. Seitenzahl,[3,4] S. Taubenberger,[2,5] G. B. Doran,[6] A. Gal-Yam,[7] R. R. Laher,[8] K. Maguire,[9] P. Nugent,[10,11] E. O. Ofek[7] and J. Surace[8]

[1]*Department of Physics and Astronomy, University of Southampton, Southampton SO17 1BJ, UK*
[2]*European Southern Observatory, Karl-Schwarzschild-Str. 2, D-85748 Garching, Germany*
[3]*ARC Centre of Excellence for All-sky Astrophysics (CAASTRO), Australian National University, Canberra, ACT 2611, Australia*
[4]*Research School of Astronomy and Astrophysics, Australian National University, Canberra, ACT 2611, Australia*
[5]*Max-Planck-Institut für Astrophysik, Karl-Schwarzschild-Str. 1, D-85741 Garching, Germany*
[6]*Jet Propulsion Laboratory, California Institute of Technology, Pasadena, CA 91109, USA*
[7]*Benoziyo Center for Astrophysics, Weizmann Institute of Science, 76100 Rehovot, Israel*
[8]*Spitzer Science Center, California Institute of Technology, M/S 314-6, Pasadena, CA 91125, USA*
[9]*Astrophysics Research Centre, School of Mathematics and Physics, Queens University Belfast, Belfast BT7 1NN, UK*
[10]*Department of Astronomy, University of California, Berkeley, CA 94720-3411, USA*
[11]*Lawrence Berkeley National Laboratory, 1 Cyclotron Road, MS 50B-4206, Berkeley, CA 94720, USA*

Accepted 2017 March 16. Received 2017 January 23; in original form 2016 October 14

ABSTRACT

We present late-time optical *R*-band imaging data from the Palomar Transient Factory (PTF) for the nearby Type Ia supernova SN 2011fe. The stacked PTF light curve provides densely sampled coverage down to $R \simeq 22$ mag over 200–620 d past explosion. Combining with literature data, we estimate the pseudo-bolometric light curve for this event from 200 to 1600 d after explosion, and constrain the likely near-infrared (Near-IR) contribution. This light curve shows a smooth decline consistent with radioactive decay, except over ∼450 to ∼600 d where the light curve appears to decrease faster than expected based on the radioactive isotopes presumed to be present, before flattening at around 600 d. We model the 200–1600 d pseudo-bolometric light curve with the luminosity generated by the radioactive decay chains of ^{56}Ni, ^{57}Ni and ^{55}Co, and find it is not consistent with models that have full positron trapping and no infrared catastrophe (IRC); some additional energy escape other than optical/near-IR photons is required. However, the light curve is consistent with models that allow for positron escape (reaching 75 per cent by day 500) and/or an IRC (with 85 per cent of the flux emerging in non-optical wavelengths by day 600). The presence of the ^{57}Ni decay chain is robustly detected, but the ^{55}Co decay chain is not formally required, with an upper mass limit estimated at 0.014 $M_\odot$. The measurement of the ^{57}Ni/^{56}Ni mass ratio is subject to significant systematic uncertainties, but all of our fits require a high ratio >0.031 (>1.3 in solar abundances).

Key words: supernovae: general – supernovae: individual: SN 2011fe.

1 INTRODUCTION

Type Ia supernovae (SNe Ia) have assumed a major role in cosmology as standardizable candles over the last 20 yr (Perlmutter et al. 1998; Riess et al. 1998) and continue to attract considerable interest as astrophysical phenomena in their own right. Although decades of intensive study have led to significant breakthroughs in our understanding of these systems, many questions remain unanswered (see the review of Howell 2011). Perhaps the most important is the underlying physical mechanism that leads to the explosion (Hillebrandt & Niemeyer 2000; Hillebrandt et al. 2013), including the configuration of the progenitor system. There is a general theoretical and observational consensus that SNe Ia are caused by the explosive thermonuclear burning of the degenerate material (Hoyle & Fowler 1960) of a carbon–oxygen white dwarf star (Nugent et al. 2011; Bloom et al. 2012) in a binary system, with the light curve primarily sustained by the radioactive decay of ^{56}Ni synthesized in the explosion (Colgate & McKee 1969; Kuchner et al. 1994; Churazov et al. 2014). The nature of the companion star to the white dwarf, however, remains uncertain (see review of Maoz, Mannucci & Nelemans 2014).

⋆ E-mail: g.dimitriadis@soton.ac.uk

The two most widely discussed classical scenarios for the progenitor system are the single degenerate (SD) scenario, where the binary consists of the accreting white dwarf with a non-degenerate companion star (Whelan & Iben 1973), and the double degenerate (DD) scenario, where the explosion originates from the 'merger' of two white dwarfs (Iben & Tutukov 1984; Webbink 1984). There continues to be significant debate in the literature as to the relative frequency of the two channels. A promising approach to distinguish the competing scenarios is the study of SNe Ia at late times via extremely late-time photometry (Röpke et al. 2012).

The shape of a SN Ia bolometric light curve is driven by the energetic output of the radioactive decay and the opacity of the (homologously) expanding ejecta into which the decay energy is deposited. The principal contributor for the first few hundred days after explosion is ^{56}Co, generated from the decay of the most abundant radioactive synthesized nuclide, ^{56}Ni. Most of the energy in the decay of ^{56}Co is emitted in the form of γ-rays and the rest in charged leptons, such as positrons and electrons, both of which are thermalized in the expanding ejecta, creating optical and near-infrared (near-IR) photons. As the ejecta expand and the column density decreases as t^{-2}, the ejecta become transparent to the high-energy γ-rays which increasingly escape thermalization. This leads to an observed light curve decline that is faster than that expected from the radioactive decay, until, after about 75–250 d (Childress et al. 2015), the contribution of positrons/electrons becomes dominant (e.g. Arnett 1979) and the bolometric light curve is expected to settle on to a decline broadly matching that of ^{56}Co. This assumes that the majority of charged leptons get trapped in the ejecta; the extent to which these get trapped is uncertain (e.g. Cappellaro et al. 1997; Milne, The & Leising 2001), but models with full positron/electron trapping are consistent with the late-time optical/near-IR observations of several SNe Ia (e.g. Sollerman et al. 2004; Stritzinger & Sollerman 2007; Leloudas et al. 2009; Graur et al. 2016).

At even later epochs, other longer lived decay chains may also contribute, in particular the chains of ^{57}Ni and ^{55}Co (Seitenzahl, Taubenberger & Sim 2009; Röpke et al. 2012). Both chains have decay steps with half-lives of several hundred days, longer than ^{56}Co, leading to a slowly declining energy input and thus a predicted flattening in very late-time (>500–600 d) SN Ia light curves. The first evidence for such nuclides has been claimed for the nearby SN Ia SN 2012cg (Graur et al. 2016), and a slow-down in the decline of the optical/near-IR light curves has been observed in other SNe Ia after ∼600 d (Cappellaro et al. 1997; Sollerman et al. 2004; Leloudas et al. 2009). Spectral modelling of the late-time SN 2011fe spectra also seems to require additional energy input from ^{57}Co (Fransson & Jerkstrand 2015).

In principle, an accurate determination of the mass of these other longer lived nuclides provides a promising diagnostic tool to distinguish between different explosion mechanisms and, in turn, different progenitor scenarios. Theoretical modelling shows that models with burning at higher central white dwarf densities predict higher ^{57}Ni/^{56}Ni mass ratios, since ^{57}Ni is a neutron-rich isotope that is produced in greater abundance in neutron-rich environments, such as near-Chandrasekhar mass explosion models. Lower central density models, such as white dwarf mergers, generally predict lower ratios (e.g. see Röpke et al. 2012; Seitenzahl et al. 2013).

A major complication is the accurate determination of the bolometric light curve. A robust theoretical prediction is the 'infrared catastrophe' (IRC), a predicted thermal instability that occurs at ∼500 d after maximum light (Axelrod 1980). During the nebular phase up until the onset of any IRC, cooling of the SN ejecta results from optical and near-IR transitions, dominated by Fe II and Fe III. However, as the ejecta expand and the temperature decreases, at ∼2000 K the cooling is instead predicted to become dominated by fine structure lines in the mid-IR with excitation temperatures of ∼500 K. This is predicted to result in rapid cooling, and the thermal emission moving from the optical/near-IR to the mid/far-IR; only ∼5 per cent of the deposited energy would emerge in the optical/near-IR at 1000 d after maximum light (Fransson & Jerkstrand 2015).

This rapid decrease in luminosity in the optical/near-IR has never been observed in SN Ia light curves (e.g. Sollerman et al. 2004; Leloudas et al. 2009), which is not consistent with predictions from model light-curve codes (Kozma & Fransson 1998a,b). The reason is unclear. One possibility is that at least a part of the SN ejecta is kept at temperatures above that at which the IRC occurs due to clumping in the ejecta (Leloudas et al. 2009). Lower density regions cool more slowly and may therefore remain above the limit for the IRC, thus maintaining some flux output in the optical/near-IR. Another possibility is that optical/near-IR luminosity can be maintained by a redistribution of ultraviolet (UV) flux into the optical wavebands, due to non-local scattering and fluorescence (Fransson & Jerkstrand 2015). Other possible complications include 'freeze-out' (Fransson & Kozma 1993), where the assumption that radiated luminosity is equal to the deposition of energy from radioactive decay breaks down.

The number of SNe Ia with the high-quality late-time data needed to make progress with these issues remains small: events must be both very nearby and (ideally) suffer from only minimal absorption from dust along the line-of-sight, keeping them visible in the opticalwavelength until very late times. Moreover, it is advantageous if the SN is located in the outskirts of its host galaxy, avoiding possible crowding from nearby stars and simplifying the photometry at late times. In this paper, we study the late-time light curve of SN 2011fe (Nugent et al. 2011), a low-extinction and spectroscopically normal SN Ia in the face-on spiral galaxy M101 located at a distance of 6.4 Mpc (Shappee & Stanek 2011). The event has a remarkably rich data set, making it the most well-studied SN Ia to date (see Kasen & Nugent 2013, for a review of the early scientific results from studies of SN 2011fe), with excellent spectroscopic (Nugent et al. 2011; Parrent et al. 2012; Foley & Kirshner 2013; Patat et al. 2013; Pereira et al. 2013; Shappee et al. 2013; Mazzali et al. 2014, 2015; Graham et al. 2015; Taubenberger et al. 2015) and photometric (Matheson et al. 2012; Richmond & Smith 2012; McClelland et al. 2013; Munari et al. 2013; Tsvetkov et al. 2013; Shappee et al. 2016; Zhang et al. 2016) coverage. Some late-time photometric studies of SN 2011fe have already been performed (Kerzendorf et al. 2014; Shappee et al. 2016; Zhang et al. 2016), and here we present new data on SN 2011fe from late-time monitoring by the Palomar Transient Factory (PTF), combined with other ground-based and *Hubble Space Telescope* (*HST*) data up until around 1600 d after peak brightness.

In Section 2, we briefly introduce SN 2011fe and describe the new measurements of its light curve from PTF and the data reduction techniques employed. In Section 3, we present the late-time PTF light curve and describe how we construct a pseudo-bolometric light curve. We introduce our analysis framework in Section 4, including correcting for photons emitted at near-IR wavelengths, and present models for the bolometric light curve, including evidence for the ^{57}Ni decay chain. In Section 5, we discuss the implications of our study. Throughout this paper, we adopt the AB magnitude system and a Hubble constant of $H_0 = 70\,\mathrm{km\,s^{-1}\,Mpc^{-1}}$.

2 DATA

Our first task is to compile a complete photometric and spectroscopic data set on SN 2011fe. In this section, we discuss SN 2011fe itself, and then the new observations presented in this paper, i.e. a new late-time light curve from the PTF survey. We also describe the significant amount of photometric and spectroscopic data that we use from the literature.

2.1 SN 2011fe and the PTF light curve

SN 2011fe was discovered by PTF at MJD 55797.2, at an apparent magnitude of $g = 17.3$ mag. Fits to the early time data give an inferred epoch for the emergence of the first photons of MJD 55796.687 $\pm$ 0.014 (Nugent et al. 2011). The SiFTO light-curve fitter (Conley et al. 2008) measures a stretch of 0.98 $\pm$ 0.01 and a $B - V$ colour at maximum light of -0.07 ± 0.02 mag (Mazzali et al. 2014), together with an epoch of maximum light in the rest-frame B band of 55814.30 $\pm$ 0.06 (2011 September 10.4 UT); all phases in this paper are given relative to this epoch. These numbers are all indicative of a normal SN Ia. The SALT2 light-curve fitter (Guy et al. 2007) gives similar results (Pereira et al. 2013). The Milky Way extinction was $E(B - V)_{\rm MW} = 0.009$ mag, and a measurement of the host galaxy extinction along the line-of-sight to the SN gives $E(B - V)_{\rm host} = 0.014 \pm 0.002$ mag (Patat et al. 2013).

The PTF (Law et al. 2009; Rau et al. 2009) was a rolling, wide-field transient survey, operating from 2009 to 2012, using the CFH12k camera (Rahmer et al. 2008) mounted on the Samuel Oschin 48-inch telescope at the Palomar Observatory (P48). The typical cadence of the survey was from hours up to 5 d, with data mostly taken in a Mould R-band filter $R_{\rm P48}$ interspersed with some g-band ($g_{\rm P48}$) observations. The limiting magnitude in good conditions was around $R_{\rm P48} \simeq 20.5$ mag. Although SN 2011fe exploded during the PTF survey, it continued to be monitored after 2012 by the intermediate Palomar Transient Factory (iPTF) experiment. The iPTF coverage began on 2013 January 1, at a phase of $\simeq$480 d. All the PTF and a portion of the iPTF data we analyse are publicly available through the Infrared Science Archive at Infrared Processing and Analysis Center (IPAC).[1]

For the PTF light curve of SN 2011fe, we employ a pipeline used extensively in earlier PTF papers (see e.g. Ofek et al. 2014; Firth et al. 2015, for particular details). The pipeline is based around a classical image-subtraction concept. A deep reference image is constructed using data prior to the first detection of SN 2011fe, which is then photometrically aligned, astrometrically registered and resampled to each image containing the SN light (the science image). The point spread function (PSF) of the resampled and science images is determined from isolated point sources in the images, and the image with the best seeing is degraded to match the PSF in the worst seeing image, using a similar technique to that of Bramich (2008). The reference image is then subtracted from the science image, producing a 'difference' image containing only objects that have changed their flux level between the reference and science image epochs.

The SN position is then measured from the difference images that have a very high signal-to-noise (S/N) of the SN, and then PSF-fitting photometry measured at this fixed position in all images after the SN was first detected, calibrating to nearby stars from the Sloan Digital Sky Survey (York et al. 2000) Data Release 12 (Alam et al. 2015). Note that SN 2011fe was bright enough to saturate the PTF camera when around peak brightness, and these saturated images are discarded from our analysis. The bulk of the data were taken in the $R_{\rm P48}$ filter (although $g_{\rm P48}$ data were also taken around maximum light), and thus we restrict the PTF analysis to $R_{\rm P48}$ in this paper. Our PTF light curve of SN 2011fe is given in Table A1, covering 819 $R_{\rm P48}$ images over PTF and iPTF, with typical science, reference and difference images, shown in Fig. 1.

[1] http://irsa.ipac.caltech.edu/

2.2 Co-adding the PTF data

SN 2011fe is clearly detected in individual PTF images up until around 400 d after maximum light. After these epochs, the data measured from the individual images, with typical 60 s exposure times, are mostly formal non-detections (i.e. $<3\sigma$ significance in any individual frame). However, much deeper limits can be reached by co-adding the PTF data to increase the sensitivity. This technique has previously been used on PTF data to successfully detect precursor events to core collapse SNe that lie below the formal detection limit of PTF (Ofek et al. 2013, 2014; Corsi et al. 2014; Strotjohann et al. 2015).

There are several choices as to how to perform this co-adding. The individual science images could be co-added prior to image subtraction; the individual difference images could be co-added prior to the photometric measurement; or the co-adding can be performed on the individual photometric data points produced by the pipeline. The first two of these options have a significant disadvantage, in that the PSF size and shape in the individual images may change significantly over the averaging period, which may last up to several tens of nights. Thus we instead choose to average the individual flux measurements made from each PTF observation.

In order to test the fidelity of the subtraction pipeline at these faint flux levels, we insert artificial SNe ('fakes') into the unsubtracted science images, and then test how accurately these fluxes can be recovered after image subtraction and averaging of the PSF photometric measurements. We inserted 2300 fake point sources at random positions, but with each fake having the same magnitude in each frame chosen to lie over the range $19 < R_{\rm P48} < 24$. We then run the image subtraction pipeline on all images, and measure the PSF flux of the fake SNe in each individual frame. These individual measurements are then averaged together to give a final recovered magnitude, exactly as for the real SN 2011fe light curve. The result of this test is shown in Fig. 2.

The pipeline generally performs well. For the epoch range we are particularly interested in (+200 to +700 d), when SN 2011fe is expected to be at $R_{\rm P48} \simeq 19$–22, we calculate a mean offset of -0.006 with a 0.019 1σ standard deviation. The outliers on the distribution are found mainly on the fainter side of the magnitude space, especially at mag>21, where naturally the pipeline underperforms.

2.3 Other data

In addition to the new PTF light-curve data for SN 2011fe, we also use complementary photometric data from other sources. In particular, we use data from Tsvetkov et al. (2013) from the Crimean Astrophysical Observatory out to $\sim$600 d, and imaging from the Gemini-N telescope from Kerzendorf et al. (2014) at around $\sim$900 d, for which we make no attempt to correct for any background light and use it as published. We also use photometric data from the Large Binocular Telescope (LBT) at $\sim$500–1600 d and *HST* imaging from

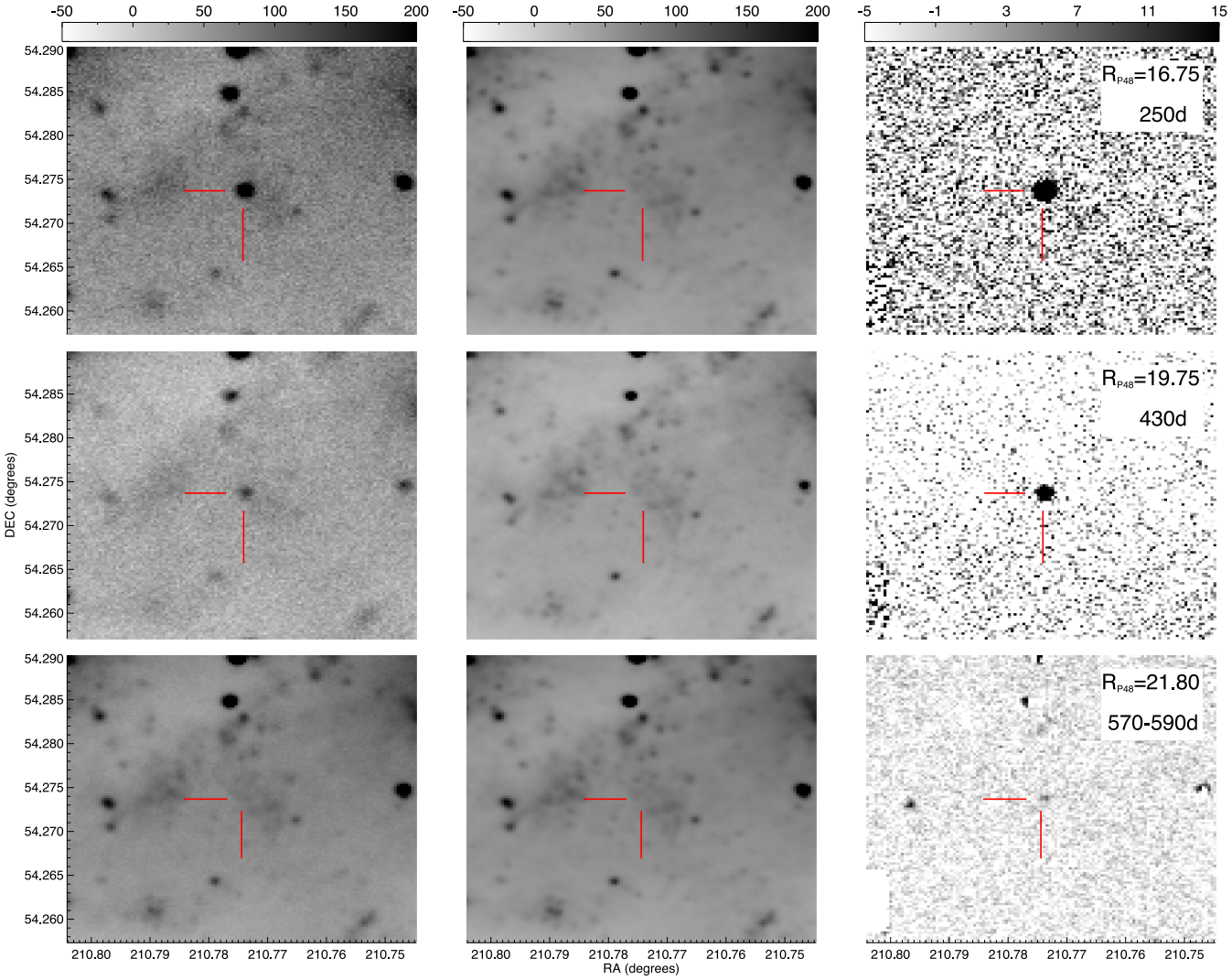

Figure 1. Late-time images of SN 2011fe. The left-hand column shows the science image, the centre column the reference image and the right-hand column the difference image. The corresponding phases of SN 2011fe (top to bottom) are +250 d, +430 d and an average of 40 images over 570–590 d, with the measured R_{P48} magnitudes indicated on the figure. The reference images indicate a low surface brightness of M101 at the position of the SN (see also the pre-explosion *HST* imaging presented in Li et al. 2011).

the Shappee et al. (2016) *HST* program at epochs >1000 d (*HST* proposals 13737 and 14166).

These data are compiled together in Table 1. Note that, unlike the PTF and the LBT light curve, none of these data are based on difference imaging, i.e. there is the possibility of contamination from background light from M101. However, deep pre-explosion *HST* imaging reveals no objects within 0.2 arcsec at the position of the SN to a 3σ limit of 26.6 mag, in *F606W* (Li et al. 2011), and thus the late-time *HST* data will be only negligibly contaminated by background light.

Our analysis also requires spectroscopic data, for the calculation of *s*-corrections, in order to correct the magnitudes estimated from different telescopes and bandpasses to a common system (R_{P48}), and pseudo-bolometric luminosities. A significant amount of spectral data on SN 2011fe at late time already exist, and we use optical data from the Lick Observatory 3-m telescope, the 4.2-m William Herschel Telescope (WHT), the 10-m Keck-I and Keck-II telescopes and near-IR data from LBT. We take all spectra from the WISeREP archive[2] (Yaron & Gal-Yam 2012), and details are presented in Table 2.

3 THE LATE-TIME LIGHT CURVE OF SN 2011fe

In Fig. 3, we present the late-time photometry of SN 2011fe obtained from PTF. The PTF coverage is shown from around +200 d when the supernova was $R_{P48} \sim 16$, through to +1200 d, when the SN was not detected even in measurements averaged over several weeks. There was no PTF coverage from around +620 to +780 d, as the field was not included in the iPTF survey during this period. We also show the other ground- and space-based optical data, where we have *s*-corrected to the R_{P48} filter using the closest available spectrum. Such a procedure assumes that our spectra match the spectral energy

[2] http://wiserep.weizmann.ac.il/

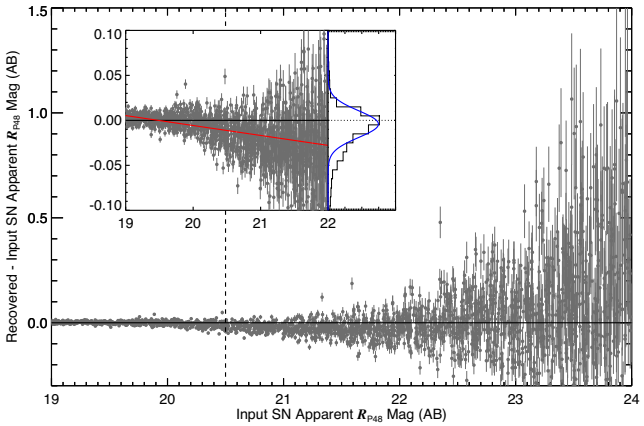

Figure 2. The fake SN tests on PTF imaging data (see Section 2.2). The main panel shows the difference between the recovered and input fake SN magnitudes for 2300 fake SNe, as a function of the input fake SN magnitude. The recovered magnitudes have been averaged over the period 200–700 d after maximum light of SN 2011fe, with the vertical error bars showing the uncertainty in the averaged magnitude. The vertical dashed line denotes the typical limiting magnitude in any individual PTF image ($R_{P48} = 20.5$). The inset shows the histogram of the magnitude differences over $19 < R_{P48} < 22$, with the best-fitting Gaussian overplotted on the histogram in blue. The red line denotes the linear correction we apply to the pipeline photometry.

distributions (SEDs) of the SN on the photometric epochs. We check this in Fig. 4, where we compare the late-time photometric $V - R$ colour of SN 2011fe with the equivalent colour calculated from the available spectra. The photometric and 'spectral' colours are consistent, with no indication of a mismatch between the colours calculated from the spectra and those from the photometry.

We identify three distinct regions of interest in the R_{P48} light curve. The first corresponds to 200–400 d, the second to 400–600 d and the third to 600–1600 d. During the first and third regions, the light curve is declining linearly in magnitude space (but with different slopes), qualitatively consistent with a light curve powered by radioactive decay. During the first period, we calculate a slope of 1.53 ± 0.09 mag per 100 d (consistent with similar studies of SNe Ia in the *R* band; see Milne et al. 2001; Lair et al. 2006) and in the third region a slope of 0.37 ± 0.12 mag per 100 d. In the second region, the light curve appears to deviate from a simple linear radioactive decay, showing a faster decline for ∼100 d followed by an apparent flattening over the next ∼50 d. The final PTF measurement is consistent with the Tsvetkov et al. (2013) *R*-band measurement at 625 d.

3.1 A pseudo-bolometric light curve

A more detailed and quantitative investigation requires a bolometric light curve covering wavelengths from UV to IR. However, there

Table 1. Literature *R*-band and near-IR photometric data for SN 2011fe.

MJD	Phase (d)[a]	Telescope	Filter	Magnitude[b]	Magnitude system	Reference
56049.50	234.93	LBT	*J*	17.18(0.10)	Vega	Shappee et al. (2016)
56257.50	442.76	LBT	*J*	17.42(0.04)	Vega	Shappee et al. (2016)
56332.50	517.70	LBT	*J*	18.23(0.18)	Vega	Shappee et al. (2016)
56337.48	522.67	LBT	*R*	22.14(0.02)	Vega	Shappee et al. (2016)
56419.46	604.59	LBT	*R*	21.74(0.03)	Vega	Shappee et al. (2016)
56440.81	625.92	1-m Crimean Astrophysical Observatory	*R*	22.00(0.12)	Vega	Tsvetkov et al. (2013)
56441.84	626.95	1-m Crimean Astrophysical Observatory	*R*	22.07(0.11)	Vega	Tsvetkov et al. (2013)
56449.21	634.32	LBT	*R*	21.91(0.02)	Vega	Shappee et al. (2016)
56453.26	638.36	LBT	*R*	21.95(0.02)	Vega	Shappee et al. (2016)
56637.53	822.48	LBT	*R*	23.19(0.04)	Vega	Shappee et al. (2016)
56743.00	927.87	GMOS-North	*r*	24.01(0.14)	AB	Kerzendorf et al. (2014)
56812.35	997.17	LBT	*R*	24.31(0.08)	Vega	Shappee et al. (2016)
56837.28	1022.08	LBT	*R*	24.54(0.08)	Vega	Shappee et al. (2016)
56839.29	1024.08	LBT	*R*	24.27(0.06)	Vega	Shappee et al. (2016)
56939.00	1123.71	*HST*	*F600LP*	24.84(0.02)	Vega	Shappee et al. (2016)
56939.00	1123.71	*HST*	*F110W*	24.30(0.04)	Vega	Shappee et al. (2016)
56939.00	1123.71	*HST*	*F160W*	22.37(0.02)	Vega	Shappee et al. (2016)
57041.51	1226.14	LBT	*R*	25.34(0.20)	Vega	Shappee et al. (2016)
57071.51	1256.11	LBT	*R*	25.46(0.14)	Vega	Shappee et al. (2016)
57118.00	1302.57	*HST*	*F600LP*	25.55(0.05)	Vega	Shappee et al. (2016)
57118.00	1302.57	*HST*	*F110W*	25.28(0.09)	Vega	Shappee et al. (2016)
57118.00	1302.57	*HST*	*F160W*	23.12(0.02)	Vega	Shappee et al. (2016)
57135.19	1319.75	LBT	*R*	25.51(0.18)	Vega	Shappee et al. (2016)
57163.23	1347.76	LBT	*R*	26.07(0.26)	Vega	Shappee et al. (2016)
57217.00	1401.52	*HST*	*F600LP*	25.82(0.04)	Vega	Shappee et al. (2016)
57217.00	1401.52	*HST*	*F110W*	25.43(0.10)	Vega	Shappee et al. (2016)
57217.00	1401.52	*HST*	*F160W*	23.41(0.04)	Vega	Shappee et al. (2016)
57389.53	1573.88	LBT	*R*	26.39(0.41)	Vega	Shappee et al. (2016)
57425.49	1609.81	LBT	*R*	26.24(0.42)	Vega	Shappee et al. (2016)
57437.50	1621.81	*HST*	*F600LP*	26.51(0.09)	Vega	Shappee et al. (2016)
57437.50	1621.81	*HST*	*F110W*	26.15(0.19)	Vega	Shappee et al. (2016)
57437.50	1621.81	*HST*	*F160W*	24.09(0.09)	Vega	Shappee et al. (2016)

[a]Assuming maximum light at MJD 55814.30 (Mazzali et al. 2014).
[b]1σ uncertainties in parentheses.

Table 2. SN 2011fe spectroscopy log.

Date (UT)	Phase (d)[a]	Telescope	Instrument	Wavelength coverage (Å)	Reference
2012 04 02	205	Lick 3-m	KAST	3440–10 268	Mazzali et al. (2015)
2012 04 23	226	Lick 3-m	KAST	3438–10 176	Mazzali et al. (2015)
2012 04 27	230	Keck-I	LRIS	3200–9991	Mazzali et al. (2015)
2012 05 01	250	LBT	Lucifer	11 700–13 100	Mazzali et al. (2015)
2012 05 01	250	LBT	Lucifer	15 500–17 400	Mazzali et al. (2015)
2012 05 01	250	LBT	Lucifer	20 500–23 700	Mazzali et al. (2015)
2012 05 26	259	WHT	ISIS	3498–9490	Mazzali et al. (2015)
2012 06 25	289	WHT	ISIS	3426–10 268	Mazzali et al. (2015)
2012 07 17	311	Lick 3-m	KAST	3458–10 254	Mazzali et al. (2015)
2012 08 23	348	Lick 3-m	KAST	3488–10 238	Mazzali et al. (2015)
2013 04 08	576	Keck-II	DEIMOS	4450–9637	Graham et al. (2015)
2014 05 01	964	Keck-I	LRIS	3077–10 328	Graham et al. (2015)
2014 06 23	1034	LBT	MODS1	3100–10 495	Taubenberger et al. (2015)

[a]Assuming maximum light at MJD 55814.30 (Mazzali et al. 2014).

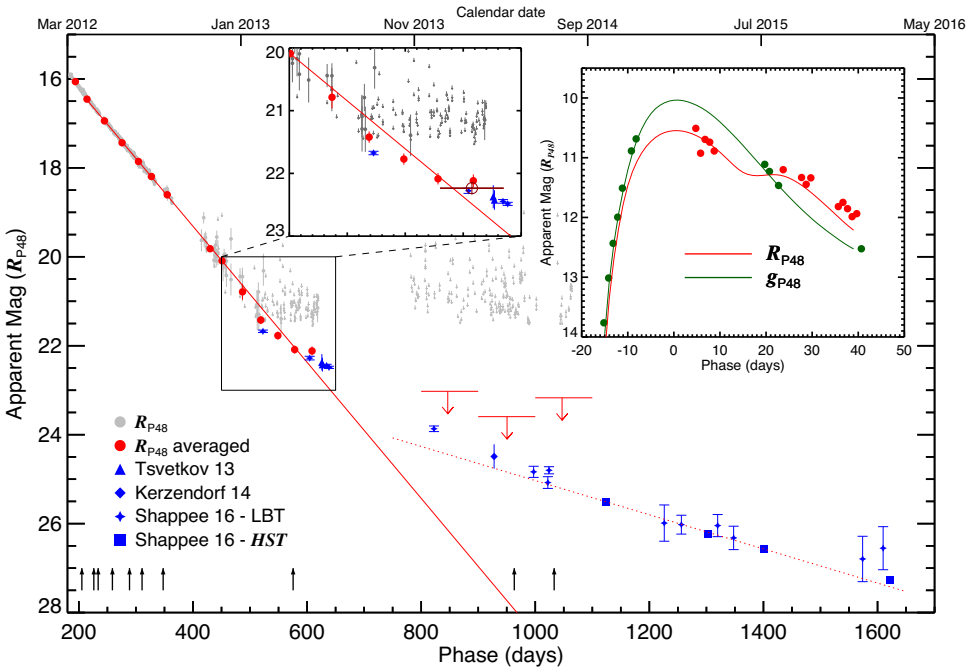

Figure 3. The SN 2011fe late-time R_{P48}-band light curve as a function of phase in days since maximum light. The light grey points show every individual PTF observation; when the significance of the detection is $<3\sigma$, an upper limit is plotted at 3σ. The red filled circles are averages of the PTF data in bins of 25 d. The literature photometric data are plotted as blue symbols and the sources are given in the legend; all are originally observed in some form of *R*-band filter (see Table 1) and *s*-corrected in the figure to R_{P48}. The black vertical arrows correspond to the epochs of the spectral sample (see Table 2). The red solid line is a linear fit over the region of +200 to +600 d, and the red dashed line a fit over +700 to +1620 d. The left inset shows a zoom of the region between +450 and +650 d, with the dark red open circle showing the averaged magnitude at the 580–640 d. The right inset shows the light curve around maximum light, together with fits from the SiFTO light-curve fitter. Uncertainties are always plotted, but are often smaller than the data points.

are few published observations in the near-IR of SN 2011fe at these late phases: the latest spectroscopic observation is at ≃250 d (Mazzali et al. 2015), while for photometric observations, available data include LBT (*J* band) and *HST* imaging, both presented in Shappee et al. (2016). Thus a true bolometric light curve is not possible to construct directly, and we restrict ourselves to constructing a bolometric light curve based only on the optical data where good spectral coverage does exist, which we hereafter refer to as a 'pseudo'-bolometric light curve. We then correct for the likely near-IR contribution in our models, based on data from SN 2011fe and other events, when analysing this pseudo-bolometric light curve. We describe the pseudo-bolometric light curve in this section.

Table 2 describes the published spectral data available, and three of these late-time spectra, at 348, 576 and 1034 d, are shown in Fig. 5. We introduce two pseudo-bolometric box filters, a wide 'BFW' filter from 3550–9500 Å and a slightly narrower 'BFN' filter covering 4500–9500 Å. The narrower BFN filter is designed for the narrower wavelength coverage of the 576 d spectrum. These two filter responses are also shown in Fig. 5, together with the R_{P48} filter response. The spectral features clearly evolve over these phases, principally with the disappearance of the [Fe III] line at 4700 Å. Most relevant for the R_{P48} filter is the weakening of the 7200 Å feature relative to the other stronger lines at bluer wavelengths (see Taubenberger et al. 2015).

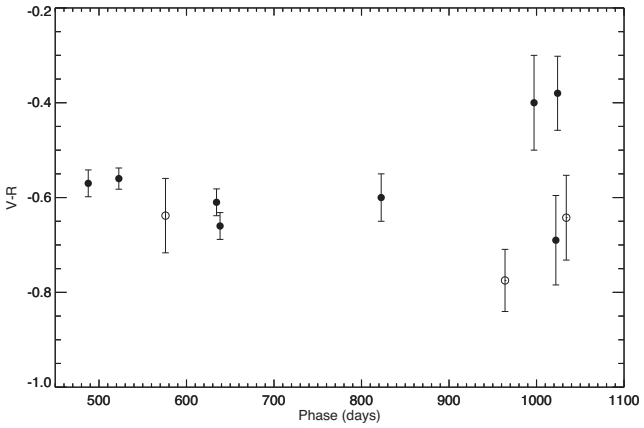

Figure 4. The $V - R$ colour of SN 2011fe at late times. Full black circles are the photometric LBT colour from Shappee et al. (2016) and open black circles denote the spectroscopic colour of the 576, 964 and 1034 d spectra (see Table 2).

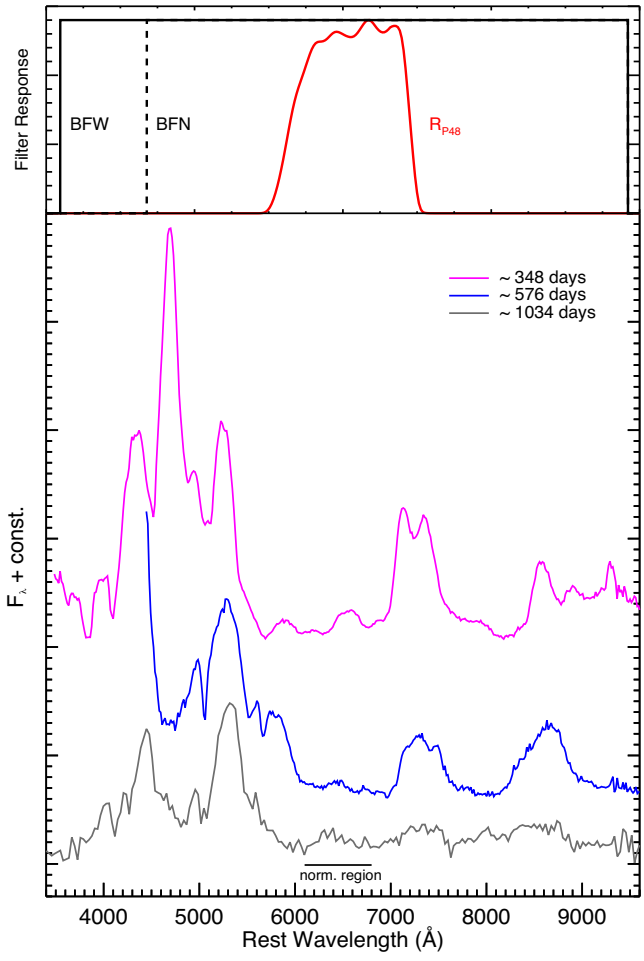

Figure 5. Lower panel: comparison of three late-time optical spectra of SN 2011fe at (from top to bottom) 348, 576 and 1034 d. Upper panel: the filter responses of the R_{P48} filter (red), the wide bolometric box filter (BFW; solid black) and the narrow bolometric box filter (BFN; dashed black).

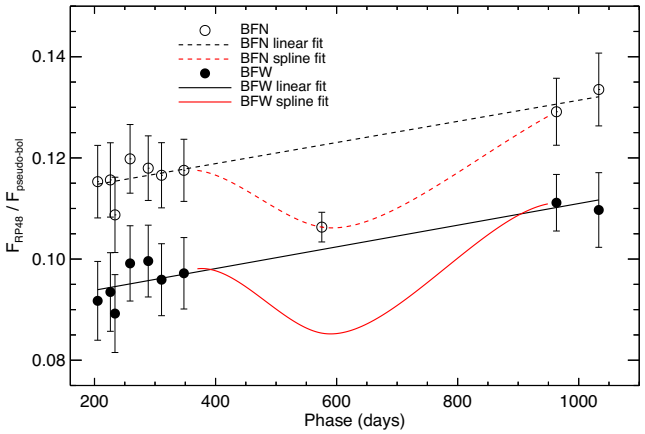

Figure 6. The ratio of the flux in the R_{P48} filter to that in the BFN filter (open circles) and the BFW filter (filled circles) for the spectral sequence in Table 2. Overplotted are the linear (black) and spline (red) fits for the BFN filter (dashed lines) and the BFW filter (solid lines). The BFW spline is a rescaled version of the BFN fit, and is not independent.

We flux calibrate the spectra in Table 2 by estimating the R_{P48} magnitude on the epoch of the spectral observation using linear interpolation. For the +576 d spectrum that coincides with the apparent break in the light curve, we average the photometry from +550 to +650 d instead of using the linear interpolation. We rescale each spectrum so that it reproduces the estimated R_{P48} apparent magnitude when integrated through that filter, and then measure the pseudo-bolometric fluxes by integrating through the BFW or BFN filters as appropriate. This is, essentially, a flux-space 'bolometric correction' for the R_{P48} data determined on each epoch on which a spectrum exists.

We then extend the bolometric corrections made on epochs on which spectra exist, to any epoch on which we have R_{P48} data. To do this we check the stability of the bolometric correction by plotting the ratio of the flux in R_{P48} to the flux in the BFW and BFN filters in Fig. 6. The two ratios evolve slowly as a function of time, with the relative flux in the R_{P48} filter generally increasing. The exception to the trend is the data point from the spectrum at +576 d in the BFN filter, where there is an apparent drop in the ratio. This is temporally coincident with the apparent break in the R_{P48}-band light curve (Fig. 3).

We fit a simple smooth spline function to the BFN ratio data to interpolate over this time period, superimposed on a linear fit to the remaining epochs for interpolation at other epochs (Fig. 6). We scale this spline fit to the BFW data, and combined with a linear fit to the other BFW data. This process allows us to translate the R-band data on any epoch into a pseudo-bolometric luminosity, and thus construct a pseudo-bolometric light curve. This light curve is shown in Fig. 8 and presented in Table 3.

4 ANALYSIS

We now turn to the analysis of the radioactive decay chains that may explain the shape and evolution of the pseudo-bolometric light curve of SN 2011fe. Our goals in this section are twofold. The first goal is to confirm that the shape of the pseudo-bolometric light curve can be explained in terms of the radioactive decay chains that are expected to be present, including ^{57}Co and ^{55}Fe (e.g. Seitenzahl, Timmes & Magkotsios 2014; Graur et al. 2016; Shappee et al. 2016). The second goal is to attempt to robustly determine the relative

Table 3. The SN 2011fe pseudo-bolometric luminosity light curve.

Phase (d)	$\log_{10}(L)$ (erg s^{-1})	Source (see Section 3.1 for details)
205.00	40.676(0.035)	Spec – Mazzali et al. (2015)
212.92	40.616(0.024)	Phot – R_{P48}
226.00	40.532(0.033)	Spec – Mazzali et al. (2015)
237.99	40.514(0.034)	Phot – R_{P48}
259.00	40.312(0.037)	Spec – Mazzali et al. (2015)
262.75	40.308(0.025)	Phot – R_{P48}
287.20	40.151(0.026)	Phot – R_{P48}
289.00	40.118(0.042)	Spec – Mazzali et al. (2015)
311.00	40.002(0.039)	Spec – Mazzali et al. (2015)
311.91	39.991(0.027)	Phot – R_{P48}
331.12	39.872(0.027)	Phot – R_{P48}
348.00	39.779(0.045)	Spec – Mazzali et al. (2015)
354.90	39.732(0.028)	Phot – R_{P48}
420.32	39.333(0.030)	Phot – R_{P48}
440.69	39.218(0.031)	Phot – R_{P48}
456.88	39.102(0.031)	Phot – R_{P48}
486.84	38.892(0.032)	Phot – R_{P48}
516.39	38.663(0.033)	Phot – R_{P48}
522.67	38.546(0.034)	Phot – Shappee et al. (2016)
536.90	38.548(0.034)	Phot – R_{P48}
562.54	38.430(0.035)	Phot – R_{P48}
576.00	38.399(0.035)	Spec – Graham et al. (2015)
585.51	38.450(0.036)	Phot – R_{P48}
604.59	38.320(0.037)	Phot – Shappee et al. (2016)
610.98	38.390(0.037)	Phot – R_{P48}
625.92	38.278(0.037)	Phot – Tsvetkov et al. (2013)
626.95	38.257(0.037)	Phot – Tsvetkov et al. (2013)
634.32	38.247(0.038)	Phot – Shappee et al. (2016)
638.36	38.230(0.038)	Phot – Shappee et al. (2016)
822.48	37.604(0.045)	Phot – Shappee et al. (2016)
927.87	37.382(0.050)	Phot – Kerzendorf et al. (2014)
964.00	37.273(0.051)	Spec – Graham et al. (2015)
1034.00	37.056(0.058)	Spec – Taubenberger et al. (2015)
1123.71	36.897(0.066)	Phot – Shappee et al. (2016)–*HST*
1302.57	36.602(0.075)	Phot – Shappee et al. (2016)–*HST*
1401.52	36.453(0.087)	Phot – Shappee et al. (2016)–*HST*
1621.81	36.163(0.100)	Phot – Shappee et al. (2016)–*HST*

amounts of ^{56}Co, ^{57}Co and ^{55}Fe that are required to reproduce the pseudo-bolometric light-curve evolution. We first introduce the framework of our modelling and the assumptions, then discuss our procedures for adjusting the model luminosity to account for near-IR contributions and finally fit the pseudo-bolometric light curve.

4.1 Analysis framework

Several different decay chains may contribute at different levels during the time period that we are sampling. These produce not only γ-rays and positrons but also electrons and X-rays that can be thermalized and deposit their energy in the expanding SN ejecta. At the late-time epochs that we study here, when the SN ejecta become increasingly optically thin, the delay between the energy deposition from the radioactive decay and the emission of optical radiation becomes short, and the light-curve time-scale becomes driven by the various decay chains.

We consider three decay chains that are likely to contribute to the bolometric output:

$$^{56}\mathrm{Ni} \xrightarrow{t_{1/2}=6.08\,\mathrm{d}} {}^{56}\mathrm{Co} \xrightarrow{t_{1/2}=77.2\,\mathrm{d}} {}^{56}\mathrm{Fe}, \quad (1)$$

Table 4. Radioactive decay constants and energies per decay.

Nucleus	λ_A (d^{-1})	q^γ (keV)	q^x (keV)	q^l (keV)[a]
^{56}Co	8.975e-3	3606.0	1.587	124.61
^{57}Co	2.551e-3	121.6	3.6	17.814
^{55}Fe	6.916e-4	–	1.635	3.973

[a]Including e^+, Auger e^- and IC e^-.

$$^{57}\mathrm{Ni} \xrightarrow{t_{1/2}=35.6\,\mathrm{h}} {}^{57}\mathrm{Co} \xrightarrow{t_{1/2}=271.2\,\mathrm{d}} {}^{57}\mathrm{Fe}, \quad (2)$$

$$^{55}\mathrm{Co} \xrightarrow{t_{1/2}=17.53\,\mathrm{h}} {}^{55}\mathrm{Fe} \xrightarrow{t_{1/2}=999.67\,\mathrm{d}} {}^{55}\mathrm{Mn}, \quad (3)$$

where the half-life is given in each case. Note that in each of these chains, one of the decay steps is significantly longer than the other; thus we make the approximation that only ^{56}Co, ^{57}Co and ^{55}Fe are important in our late-time ($t > 200$ d) light-curve analysis (we neglect other decay chains such as ^{44}Ti as they will be subdominant for many years; e.g. Seitenzahl et al. 2009).

Under these approximations, the bolometric luminosity L for a given decay chain is

$$L_A(t) = \frac{2.221}{A}\frac{\lambda_A}{\mathrm{d}^{-1}}\frac{M(A)}{\mathrm{M}_\odot}\frac{q_A^\mathrm{l} f_A^\mathrm{l}(t) + q_A^\gamma f_A^\gamma(t) + q_A^\mathrm{x}}{\mathrm{keV}} \times \exp(-\lambda_A t) \times 10^{43}\,\mathrm{erg\,s^{-1}}, \quad (4)$$

where t is the time since explosion, A is the atomic number of the decay chain, $M(A)$ is the initial mass synthesized, λ_A is the decay constant, q_A^l, q_A^γ and q_A^x are the average energies per decay carried by the (electrically charged) leptons, γ-rays and X-rays and f_A^l and f_A^γ are the fractions of the leptons and γ-rays absorbed in the ejecta, i.e. that contribute to the luminosity. Under the assumption of homologous expansion, these fractions are time dependent and are given by

$$f_A^{\mathrm{l},\gamma}(t) = 1 - \exp\left[-\left(\frac{t_A^{\mathrm{l},\gamma}}{t}\right)^2\right], \quad (5)$$

where $t_A^{\mathrm{l},\gamma}$ corresponds to the time when the optical depth, $\tau_A^{\mathrm{l},\gamma}$, for positrons/leptons or γ-rays becomes unity, i.e. $\tau_A^{\mathrm{l},\gamma} = (t_A^{\mathrm{l},\gamma}/t)^2$. In this framework, the effective opacity for each species, $k_A^{\mathrm{l},\gamma}$, is proportional to t_A^2. Under the leptonic contribution channel, we include positrons, Auger and internal conversion electrons.

The values for the decay energies and constants are presented in Table 4, and can be found at the National Nuclear Data Center.[3]

In our analysis, we make the following simplifications.

(i) We fix $t_{56}^\gamma = 35$ d. This parameter is not well measured by our late-time pseudo-bolometric light curve, but is well constrained in the literature. Sollerman et al. (2004), Stritzinger & Sollerman (2007) and Leloudas et al. (2009) have calculated t_{56}^γ for SN 2000cx, SN 2001el and SN 2003hv to be $t_{56}^\gamma = 31.5$, 35 and 32.5 d, respectively, while Zhang et al. (2016) infer $t_{56}^\gamma = 34.5$ d for SN 2011fe. We include the (small) contribution to the heating from ^{56}Co γ-rays even at very late times.

(ii) We fix $t_{57}^\gamma = 160$ d. This parameter is, again, not well measured. The main γ-ray contribution from ^{57}Co are the low-energy

[3] http://www.nndc.bnl.gov

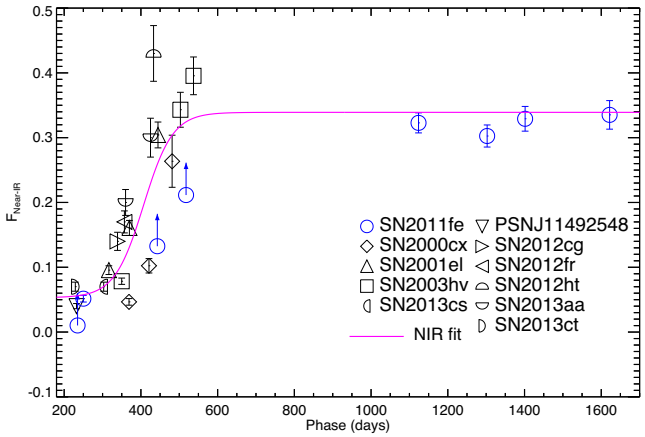

Figure 7. The near-IR contribution, $F_{\text{near-IR}}(t)$ (equation 6), for SNe Ia taken from the literature; see Section 4.2. The blue points show data for SN 2011fe. The magenta line corresponds to the functional form that we adopt in our fitting to SN 2011fe.

14.4, 122.1 and 136.5 keV lines. For the 14.4 keV, we assume complete trapping. For the 122.1 and 136.5 keV ones, we use a value for t^{γ}_{57} that suggests a 10 per cent trapping at 500 d.

(iii) We treat t^{l}_{56}, t^{l}_{57} and t^{l}_{55} as free parameters in some of the fits, i.e. we do not assume full trapping of the leptonic channel.

(iv) We assume complete trapping of the low-energy X-rays.

4.2 Non-optical contribution

Our pseudo-bolometric light curve (Section 3.1) is based on optical data only. We must therefore account for the radiation emerging at non-optical wavelengths either by correcting the data or by adjusting the model. Here we choose to adjust the model, keeping our data as close to the observations as possible.

In Fig. 7, we present the total near-IR contribution for SN 2000cx, SN 2001el and SN 2003hv based on broad-band imaging (Sollerman et al. 2004; Stritzinger & Sollerman 2007; Leloudas et al. 2009). We also use near-IR estimates based on nebular spectra of seven SNe Ia taken from Maguire et al. (in preparation) and observed in the optical and near-IR with the Very Large Telescope XShooter spectrograph. Finally, we include a point for SN 2011fe obtained by integrating the available near-IR spectrum at 250 d (Table 2), the near-IR LBT data (plotted with upward arrows, since they are only *J*-band observations) and the *HST* data from Shappee et al. (2016) at later phases. Note for the literature SNe Ia the rapidly increasing near-IR flux contribution over 400–600 d, as flux is presumably redistributed from the optical to the near-IR. This generally leads to optical light curves declining more rapidly than near-IR light curves over these epochs due to the decreasing temperature in the ejecta and the consequently increased importance of the near-IR [Fe II] lines (e.g. Sollerman et al. 2004; Leloudas et al. 2009).

The calculation of the near-IR contributions of SN 2000cx, SN 2001el and SN 2003hv is performed as follows. The published light-curve magnitudes were extinction corrected and converted to fluxes, with linear interpolation for the missing epochs. The optical fluxes were used to adjust the available spectra of SN 2011fe so that the spectra reproduce the optical colours, using the 'mangling' technique of Hsiao et al. (2007) and Conley et al. (2008), and then integrated through the 'BFW' filter (or the 'BFN' filter, adding the appropriate correction from Section 3.1), thus calculating the optical part of the bolometric light curve. The near-IR *JHK* fluxes were integrated over their effective filter area. The near-IR contribution is then defined as

$$F_{\text{nir}}(t) = \frac{L_{\text{nir}}(t)}{L_{\text{opt}}(t) + L_{\text{nir}}(t)}. \quad (6)$$

While the absolute contributions differ from SN to SN, the general shape is similar, indicating a colour evolution over ∼300–600 d that shifts flux from the optical to near-IR wavelengths. We fit a simple functional form, based on the logistic or sigmoid function, to these data to model this near-IR contribution as a function of time. While a more complex near-IR colour evolution is possible, leading to a local maximum at ≃650 d, seen in SN 2003hv (fig. 8 of Leloudas et al. 2009), we will retain this simple functional form, mainly because the last data point of SN 2003hv is based on extrapolating the light curve, under the assumption that the $J - H$ and $H - K$ colours do not change, making the final calculation highly speculative.

The final model luminosity, $L_{\text{model}}(t)$, that we fit to our pseudo-bolometric light curve is then

$$L_{\text{model}}(t) = [L_{55}(t) + L_{56}(t) + L_{57}(t)]\,[1 - F_{\text{nir}}(t)]\,, \quad (7)$$

where L_{55}, L_{56} and L_{57} are given by equation (4), and F_{nir} is determined as detailed above.

We also estimate the contribution of mid-IR emission over 500–600 d from the *Spitzer* light curve obtained with the Infrared Array Camera (IRAC) channels 1 and 2 (at 3.6 and 4.5 μm, respectively) presented in Johansson et al. (2017). We can only estimate an upper limit, but find a total mid-IR contribution of ∼1 per cent, indicating that little flux is emitted in the mid-IR region at these epochs. We defer a discussion of the far-IR region (and a possible IRC) to the next section. Finally, we note that the contribution at UV wavelengths smaller than 3500 Å is expected to be small, since it is dominated by optically thick lines, and the only SN 2011fe nebular UV spectrum shows little UV flux (Friesen et al., in preparation).

4.3 Analysis of the bolometric light curve

The late-time pseudo-bolometric light curve of SN 2011fe derived in Section 3.1 is shown in Fig. 8. In this section, we consider various model fits to this light curve and attempt to constrain the various fit parameters.

We begin by fitting equation (7), including all three decay chains (equations 1–3), directly to our data, assuming full trapping of positrons/electrons and no flux emerging at $\lambda > 2.5$ μm (Fig. 8), which we refer to as 'Case 0'. The best-fitting parameters are reported in Table 5. This provides a very poor fit to the data with a reduced χ^2 (the χ^2 per degree of freedom) of $\chi^2_{\text{DOF}} \simeq 24$ for 36 degrees of freedom. The model cannot simultaneously fit the data over 200–400 d and over 900–1600 d, and prefers a low ^{56}Ni mass ($M(56) = 0.18\ \text{M}_{\odot}$).

This $M(56)$ is significantly lower than other independent estimates. Mazzali et al. (2015) estimated $M(56) = 0.47 \pm 0.05\ \text{M}_{\odot}$ from nebular spectroscopy. Pereira et al. (2013) used the bolometric light curve around peak brightness to estimate $M(56) = (0.44 \pm 0.08) \times (1.2/\alpha)\ \text{M}_{\odot}$, where $\alpha = 1.2 \pm 0.2$ is the ratio of bolometric to radioactivity luminosities (instead assuming $\alpha = 1.0 \pm 0.2$ would give $M(56) = 0.53 \pm 0.11\ \text{M}_{\odot}$). This suggests that the model needs a way to lose energy outside of the optical/near-IR wavebands. We next consider two ways in which this could occur.

For 'Case 1', which we refer to as the 'positron/electron escape case', we allow the positron/electron escape fractions (t^{l}_{56}, t^{l}_{57})

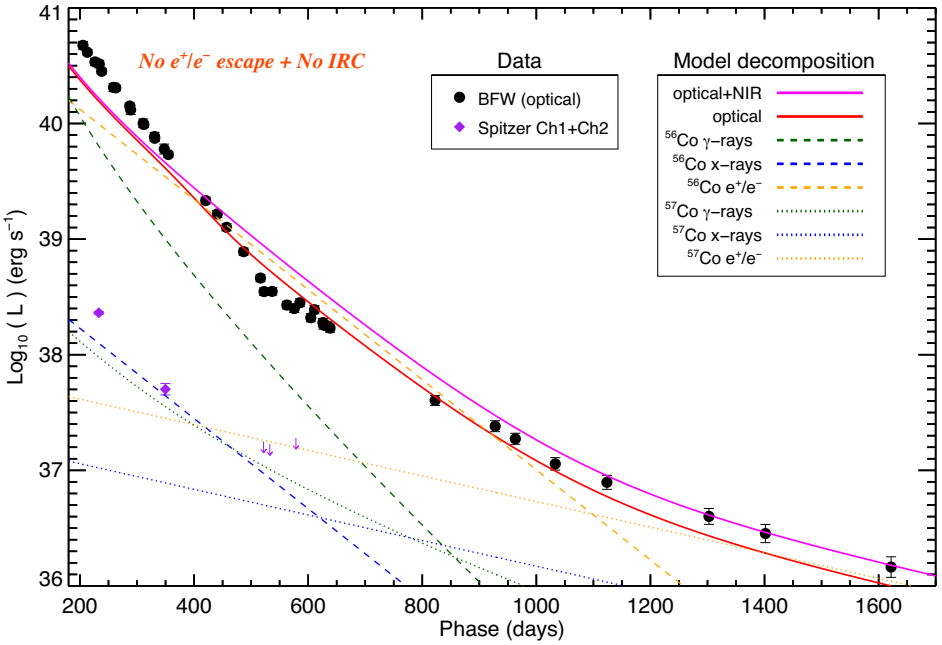

Figure 8. The pseudo-bolometric light curve of SN 2011fe shown as filled black circles; see Section 3.1 for details of the light-curve construction. This figure shows the fit of the 'Case 0' model (Section 4.3), assuming complete positron/electron trapping and no emergent far-IR flux. The magenta line is the total (optical plus near-IR) bolometric luminosity, and the red line is the final model fit to the pseudo-bolometric light-curve data based on equation (7), once the near-IR contribution is accounted for. The mid-IR *Spitzer* light curve (Johansson et al. 2017) is plotted as purple diamonds and upper limits. We include the decomposition of our model into the two decay chains of $A = 56$ and 57, separated into the γ-ray, X-ray and positron/electron components, shown in the legend.

Table 5. The best-fitting parameters for the modelling of the pseudo-bolometric light curve.

Model	$M(56)$ ($M_\odot$)	$M(57)$ ($M_\odot$)	$M(55)$ ($M_\odot$)	$M(57)/M(56)$	$M(57)/M(56)$ $(^{57}Fe/^{56}Fe)_\odot$[a]	t^1_{56} (d)	t^1_{57} (d)	χ^2_{DOF}	DOF
Case 0	0.179(0.003)	0.004(0.001)	0.0(0.0)	0.022(0.003)	0.963(0.114)	–	–	24.09	36
Case 1	0.461(0.041)	0.014(0.005)	0.0(0.0)	0.031(0.011)	1.322(0.473)	233(30)	886(427)	2.47	34
Case 1, excluding 550–650 d	0.442(0.035)	0.015(0.007)	0.0(0.0)	0.023(0.016)	1.47(0.731)	249(32)	812(551)	2.25	25
Case 2	0.355(0.017)	0.021(0.003)	0.0(0.0)	0.059(0.008)	2.571(0.346)	–	–	2.08	33
Case 2, excluding 550–650 d	0.357(0.018)	0.022(0.003)	0.0(0.0)	0.060(0.009)	2.627(0.391)	–	–	1.96	24

[a]Assuming $(^{57}Fe/^{56}Fe)_\odot = 0.023$ (Asplund et al. 2009).

to be free parameters in the fit. We then find (Table 5) $M(56) = 0.461 \pm 0.041$ $M_\odot$, $M(57) = 0.014 \pm 0.004$ $M_\odot$ and $M(55) = 0.0$ $M_\odot$, with a much improved fit quality ($\chi^2_{DOF} \simeq 2.5$ for 34 degrees of freedom, Fig. 9). This fit provides strong evidence for the presence of the ^{57}Ni decay chain. The fit also requires a considerable positron/electron escape over the phase range of 200–600 d; for example, at 500 d ≃75 per cent of the leptonic energetic output escapes the ejecta. The inferred trapping functions for this fit are shown in Fig. 10.

Our inferred ^{56}Ni mass, $M(56) = 0.461$ $M_\odot$, is consistent with other independent estimates (see above). The small difference compared to that from nebular spectroscopy (around 3 per cent) could be attributed to some part of the SED that is not covered by our pseudo-bolometric filter or near-IR correction. Generally, however, this fit provides evidence that our pseudo-bolometric light curve and the near-IR modelling are accounting for most of the emitted photons, *assuming* that the charged leptons are able to escape the ejecta.

We note that from around +500 d onwards, the optical bolometric light curve begins to decline faster, before beginning to flatten just before +600 d. This behaviour, particularly the flattening, is not well reproduced by our simple model, although the faster decline occurs at the same time as flux is being redistributed to the near-IR (Fig. 7). We therefore also fit the bolometric light curve excluding the phase range of 550–650 d, where the underlying behaviour is not well understood and shows a different apparent decay rate. The parameters are again reported in Table 5 – these are close to the original fit values, but with an improved χ^2_{DOF}.

Although we have accounted for the non-optical luminosity in our fitting up to 2.5 μm, there are strong theoretical reasons to expect significant mid/far-IR luminosity at late times due to the IRC. Therefore, in 'Case 2' we use a different approach for the non-optical contribution. Motivated by the fact that there has not been any strong observational evidence for positron/electron escape in SNe Ia, we investigate the 'IRC case', where a substantial amount of flux is shifted to far-IR wavelengths. For this, we fit a model where we force complete positron/electron trapping for the full bolometric light curve; in other words, we fix f^1_A in equation (4) to 1. This final model luminosity then will be

$$L_{model}(t) = [L_{55}(t) + L_{56}(t) + L_{57}(t)] \left[1 - F_{non\text{-}opt}(t)\right], \quad (8)$$

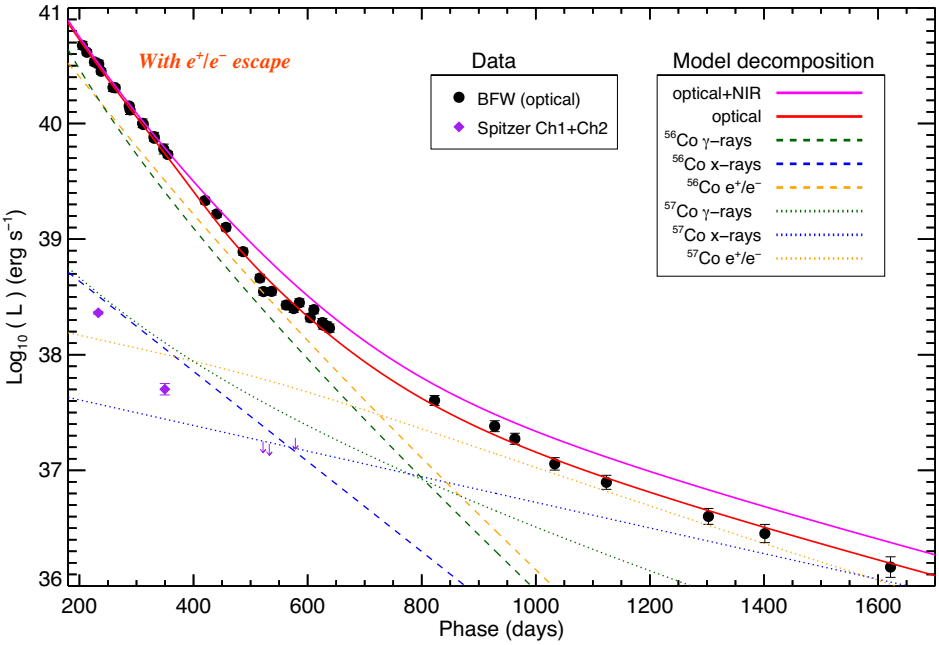

Figure 9. The pseudo-bolometric light curve of SN 2011fe shown as filled black circles; see Section 3.1 for details of the light-curve construction. This figure shows the fit of the 'Case 1' model (Section 4.3), allowing for positron/electron escape and assuming that the optical light-curve and near-IR corrections (Section 4.2) account for all of the emerging photons. Fig. 11 shows the fit of the 'Case 2' model, which does not allow positron/electron escape but instead allows for luminosity to emerge at wavelengths greater than 2.5 μm.

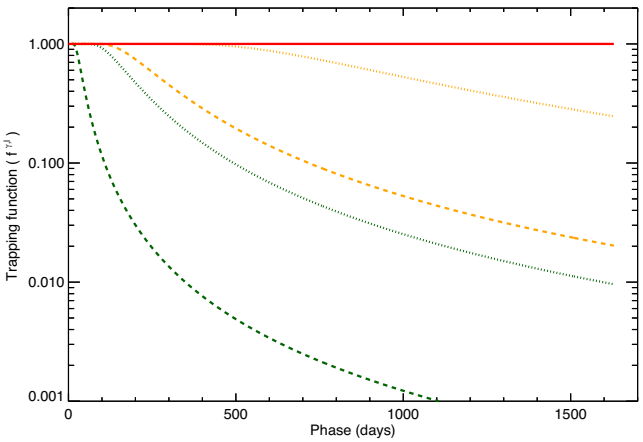

Figure 10. The inferred trapping functions for γ-rays ($f^{\gamma}(t)$) and positrons ($f^{l}(t)$), from equation (5), resulting from our 'Case 1' fits. The green lines correspond to γ-rays with $t^{\gamma}_{56} = 35$ d (dashed) and $t^{\gamma}_{57} = 160$ d (dotted) that we assume for ^{56}Co and ^{57}Co decay, respectively. The yellow lines correspond to the leptonic trapping from the ^{56}Co decay, $t^{l}_{56} = 233$ d (dashed), and the leptonic trapping for ^{57}Co decay, $t^{l}_{57} = 886$ d (dotted). The red solid line corresponds to complete trapping.

where L_{55}, L_{56} and L_{57} are given as before, by equation (4), and $F_{\rm non\text{-}opt}$ corresponds to the *total* non-optical contribution, for which we assume the same logistic functional form as in Fig. 7, but with a limit at 200 d to be $\simeq$1 per cent. We then fit for $M(56)$, $M(57)$, $M(55)$ and the total non-optical contribution. The result is plotted in Fig. 11 and again reported in Table 5.

For this fit, we find $M(56) = 0.355 \pm 0.017$ M$_{\odot}$, $M(57) = 0.021 \pm 0.003$ M$_{\odot}$ and $M(55) = 0.0$ M$_{\odot}$ with $\chi^2_{\rm DOF} \simeq 2$ for 33 degrees of freedom. We note this fit prefers a smaller $M(56)$, lower than previous estimates, indicating that at the earlier part of our bolometric light curve there still is 25 per cent of the flux that we still do not probe. Fixing instead the $M(56)$ mass to $M(56) = 0.47$ M$_{\odot}$, and allowing the non-optical contribution at 200 d to be unconstrained, we find $M(57) = 0.028 \pm 0.003$ M$_{\odot}$ and a non-optical contribution at 200 d equal to 25 per cent, with $\chi^2_{\rm DOF} \simeq 2.04$ for 34 degrees of freedom.

Our inferred non-optical contribution increases to $\simeq$85 per cent at 600 d. This is consistent with Fransson & Jerkstrand (2015), who estimated an 80 per cent non-optical/near-IR contribution at 1000 d, although their models indicate that this flux is mainly emitted in the mid-IR. In our analysis, we have assumed a constant evolution of the non-optical contributions after +600 d, the approximate expected epoch of any IRC. This assumption may not be correct, and a colour evolution that decreases the near-IR flux and increases the mid/far-IR one is certainly possible, but not constrained by our data. We note that the *Spitzer* mid-IR flux from Johansson et al. (2017) is very small, although in the event of an IRC, the theoretical prediction is that the fine-structure lines will be redward of the mid-IR *Spitzer* filter bandpass.

5 DISCUSSION

We now investigate other physical mechanisms that may contribute to the behaviour of the bolometric late-time light curve, and then discuss the implications of our study in the context of SN Ia explosion models and physics.

5.1 Other contributions to the late-time luminosity

Although our simple model provides a good fit to most of our pseudo-bolometric light-curve data, we cannot rule out other sources of luminosity that may affect the late-time light curve. We discuss these in turn (see also a similar discussion in the context of SN 2012cg in Graur et al. 2016).

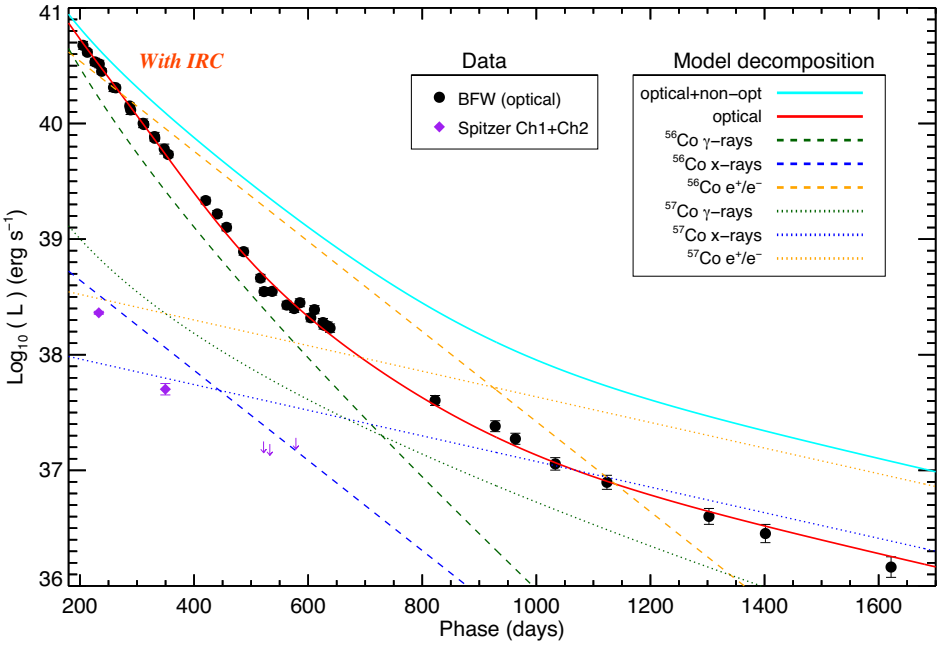

Figure 11. As Fig. 9, but for the 'Case 2' model that accounts for flux emerging at $\lambda > 2.5$ μm (i.e. an IRC) and assumes full positron/electron trapping. Here, the cyan line denotes the inferred total (optical+near-IR+mid/far-IR) bolometric light curve of the SN.

5.1.1 A light echo

The flattening of the light curve of SN 2011fe from around 600 d could be explained by the presence of a dust cloud near the SN that scatters a fraction of the SN light towards the observer, a mechanism known as 'light echo'. Due to the different light travel times, the spectrum we observe would then be an integrated combination of the scattered early-time spectra combined with the direct line-of-sight late-time spectrum. This behaviour has been demonstrated for several SNe Ia (e.g. Schmidt et al. 1994; Cappellaro et al. 2001; Drozdov et al. 2015), where the bolometric light curves evolve in a manner consistent with ^{56}Co up to >500–600 d, at which point the light curves flatten. The spectra also evolve from classical SN Ia nebular spectra over ∼300–500 d, to spectra showing a blue continuum with broad absorption and nebular emission features superimposed at ∼500–600 d. Schmidt et al. (1994) and Cappellaro et al. (2001) can reproduce the late-time SN Ia spectra with a model light-echo spectrum, constructed by co-adding early-time spectra multiplied by a power-law scattering function, $S_\lambda \propto \lambda^{-\alpha}$, with $\alpha = 1, 2$ (for a more detailed approach see Marino et al. 2015).

While the late-time photometric behaviour of SN 2011fe partly resembles a light echo (e.g. the flattening at ∼600 d), a light echo is unlikely to be responsible. The late-time spectra are considerably different from a blue-continuum light echo spectra. We demonstrate this following the procedure of Schmidt et al. (1994) and Cappellaro et al. (2001). We used the available early-time spectra of SN 2011fe from WISeREP, spanning −5 to +75 d, and after weighting them by the integrated luminosity at their observed epochs, correcting for reddening and using scattering laws as above, we co-add them constructing an expected light echo spectrum. In Fig. 12, we compare the late-time SN 2011fe spectrum with the two synthesized light echo spectra for the two different scattering laws with $\alpha = 1, 2$. We observe no similarities between the observed and synthetic spectra, and thus conclude that a light echo cannot significantly influence the SN 2011fe light curve. A similar study has been performed by Shappee et al. (2016), reaching similar conclusions.

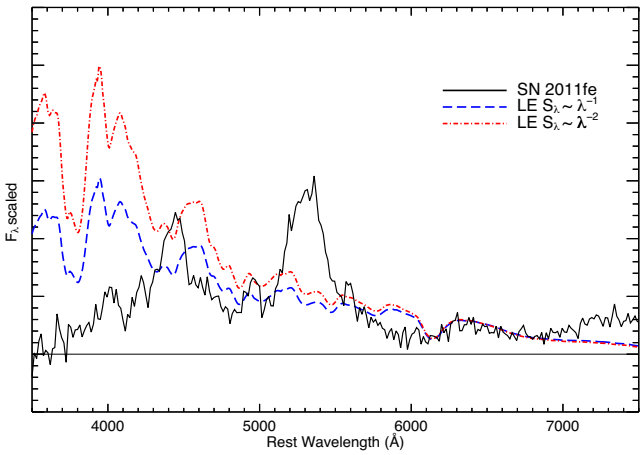

Figure 12. The +1030 d SN 2011fe spectrum (black solid line; Taubenberger et al. 2015), compared to two synthetic 'light echo' spectra constructed with scattering laws of $S_\lambda \propto \lambda^{-1}$ (blue dashed line) and $S_\lambda \propto \lambda^{-2}$ (red dashed–dotted line). For details see Section 5.1.

5.1.2 Circumstellar material

A possible explanation for the brightness of SN 2011fe at these late epochs is that the light curve is contaminated by interaction of the ejecta with circumstellar material (CSM) around the explosion. While a complete investigation of these possibilities is beyond the scope of this paper, we note that we do not see hydrogen in any of the late-time spectra, indicating little interaction with a CSM, with no hot blackbody component and no narrow/intermediate emission lines of any element.

5.1.3 A surviving companion

Finally, we consider whether a surviving binary companion could also contribute significant luminosity at late times. If we fit the

bolometric light curve with a simple ^{56}Co decline law and a constant luminosity component, simulating a surviving companion, we find $L_{\rm companion} = 7.7 \pm 0.6 \times 10^2$ L$_\odot$, with $\chi^2_{\rm DOF} \simeq 8.6$ for 36 degrees of freedom. This upper limit would be consistent with a red giant or main-sequence star of $\sim$6 M$_\odot$, but such a possibility is excluded by the analysis of the *HST* pre-explosion imaging by Li et al. (2011) and stellar evolution time-scales (however, less massive companions could have an increased luminosity due to interaction with the SN ejecta). Thus, again, this possibility seems unlikely, as was also found in Shappee et al. (2016).

5.2 Implications

5.2.1 *The infrared catastrophe or positron/electron escape?*

We next investigate whether an IRC may have occurred in SN 2011fe, and discuss the implications of this phenomenon regarding the late light-curve evolution. As discussed in the Introduction, the IRC is the result of a rapid cooling in the ejecta, with the thermal emission moving from the optical/near-IR to the mid/far-IR. There is no published direct evidence for a dramatic IRC in SN 2011fe, either in the spectroscopy, where prominent optical emission lines are still seen (e.g. Taubenberger et al. 2015), or in other photometric studies (Kerzendorf et al. 2014).

However, in this paper, we have shown that the pseudo-bolometric light curve is difficult to reconcile with the evolution expected from the ^{56}Ni and ^{57}Ni decay chains with models involving complete or nearly complete trapping of the charged leptons. Such a model can be made to be consistent with the data in the presence of significant positron/electron escape.

We note that such a positron escape is disfavoured, since it would be difficult to explain the distribution of the observed positron signal from the Milky Way. Crocker et al. (2016) determine the required age of a putative stellar source of the Galactic positrons, constrained by the recently revised positron annihilation signal of the bulge, disc and nucleus of our Milky Way (Siegert et al. 2016). Crocker et al. (2016) require the putative stellar source of the positrons to have an age of 3–6 Gyr and argue strongly against normal SNe Ia (with typical ages of 300–1000 Myr) as the main source of positrons in our Galaxy.

Therefore, taking into account the lack of any evidence for very high positron/electron escape from SNe Ia, we favour the interpretation of the late-time light-curve evolution as a redistribution of flux from the optical/near-IR to the mid/far-IR, similar to an occurrence of an IRC.

5.2.2 *Evidence for* ^{57}Ni *and* ^{55}Co

The luminosity produced by the ^{57}Ni decay chain is unambiguously detected in our analysis; fits based just on ^{56}Ni cannot reproduce the observed evolution. In principle, a measurement of the ratio of the synthesized ^{57}Ni to ^{56}Ni masses ($M(57)/M(56)$) can possibly disentangle potential explosion mechanisms, and thus provide some insight into the progenitor system. A recent demonstration on the SN Ia SN 2012cg (Graur et al. 2016) claimed $M(57)/M(56) = 1.87^{+0.52}_{-0.48}$ (here we give all ratios in terms of the solar value of $(^{57}{\rm Fe}/^{56}{\rm Fe})_\odot = 0.023$; see Asplund et al. 2009), increasing to a higher value of $2.96^{+0.83}_{-0.78}$ when enforcing $M(55) = 0$.

However, such measurements are clearly susceptible to assumptions made in the modelling, and thus systematic uncertainties. Our fit ratios range from $M(57)/M(56) = 1.3$–2.5, i.e. supersolar. These values are broadly consistent with the ratios predicted for the one-dimensional W7 (1.7; Iwamoto et al. 1999) and the two-dimensional (1.4–1.9; Maeda et al. 2010) and three-dimensional (1.3; Seitenzahl et al. 2013) delayed detonation models, but not with the violent merger (1.1; Pakmor et al. 2012) model.

While the systematic uncertainties of our modelling are large, the (simple) models that we have investigated indicate a high $M(57)/M(56)$ ratio, in contradiction with Shappee et al. (2016), pointing to an explosion mechanism with relatively high central density of synthesized ^{56}Ni. This kind of explosion mechanisms are associated with SD progenitor channels (however, see Fenn, Plewa & Gawryszczak 2016).

In all of our fits, we use a physical prior in our models that all of the synthesized masses must be greater than or equal to zero. The fits including ^{55}Co hit this limit for $M(55)$, precluding the calculation of uncertainties in this parameter. Relaxing this assumption gives a very small negative value for $M(55)$ with an uncertainty of 6.9×10^{-3} and 1.6×10^{-2} M$_\odot$ for 'Case 1' and 'Case 2', respectively. The corresponding upper limit ratios are then $M(55)/M(57) = 0.47$ and 0.56; the corresponding predicted ratios for the two-dimensional delayed detonation models are 0.4–0.6 (Maeda et al. 2010), for the three-dimensional delayed detonation model (Seitenzahl et al. 2013) the prediction is 0.7 and for the violent merger model (Pakmor et al. 2012; Röpke et al. 2012) it is 0.25.

6 CONCLUSIONS

In this paper, we have presented a late-time optical *R*-band light curve for the type Ia supernova SN 2011fe, measured using data from the PTF. Combining this light curve with other published photometric data from ground-based telescopes and the *HST*, and with ground-based spectroscopy, we have estimated the pseudo ('optical') bolometric light curve out to 1600 d after peak brightness. We also construct a model for the likely bolometric output in the near-IR. We analyse this light curve using a simple model of energy deposition from three possible decay chains (^{56}Ni, ^{57}Ni and ^{55}Co). Our main findings are the following.

(i) The bolometric light curve for SN 2011fe can be broadly explained by the radioactive inputs from the ^{56}Ni and ^{57}Ni decay chains. The presence of the ^{57}Ni decay chain is required and is robustly detected in our analysis.

(ii) The PTF *R*-band light curve has a noticeable rapid decline followed by a plateau over 500–600 d. While the rapid decline can be explained by a cooling ejecta and the emergence of [Fe II] lines producing increased near-IR flux, our simple models are unable to adequately explain the plateau feature in the light curve.

(iii) Our pseudo-bolometric light curve is not consistent with models that have full trapping of the produced charged leptons and no IRC. An additional route for energy escape outside of the optical/near-IR is required.

(iv) The bolometric light curve is consistent with models that allow for positron/electron escape. In this case, our best-fitting initial ^{56}Ni mass is $M(55) = 0.461 \pm 0.041$ M$_\odot$, consistent with independent estimates from nebular spectroscopy analysis and Arnett's law. However this model requires 75 per cent of the charged leptons to escape by 500 d.

(v) Alternatively, our data are also fully consistent with a model that has complete positron/electron trapping but does allow for a redistribution of flux to the mid-/far-IR, similar to an IRC (Axelrod 1980). In this case, around 85 per cent of the total

bolometric luminosity must be escaping at non-optical wavelengths by day 600 and onwards.

(vi) For both of these scenarios, the amount of ^{57}Ni we estimate is relatively large, compared to popular explosion models. This large inferred mass indicates high central density explosion environments, mainly predicted from SD progenitor channels and white dwarf collisions.

(vii) Including contributions from the ^{55}Co decay chain does not improve the quality of the bolometric light-curve fits, although this is not well constrained by the data set. We estimate an upper limit of ^{55}Co mass of 1.6×10^{-2} $M_{\odot}$.

This paper has highlighted the significant systematic uncertainties that are involved in modelling the late-time light curves of SNe Ia, even within a very simple framework. Even though high-quality data were obtained for SN 2011fe during the late phases, a denser time sampling of photometric and spectroscopic late-time observations spanning the optical and IR are needed for future similar events, particularly over the phase range of 400–800 d, where the ionization state appears to change and a sharp colour evolution can occur (including mid- and far-IR data where possible). We also neglected dependent effects in our modelling, such as freeze-out. While these effects are predicted to be small out to at least 900 d (Fransson & Jerkstrand 2015), more detailed modelling may provide an improved interpretation of the very late-time light curve. Repeating this study for a larger sample of events will allow us to precisely measure and compare the nickel masses obtained from peak and late times, extracting information on the energetic output of the radioactive decay and confirm whether positron escape and/or an IRC is occurring.

ACKNOWLEDGEMENTS

The authors thank Claes Fransson and Anders Jerkstrand for helpful discussions regarding the infrared catastrophe and its theoretical implications.

We acknowledge support from EU/FP7-ERC grant no. [615929] and the Weizmann–UK 'Making Connections' program. This research was supported by the Munich Institute for Astro- and Particle Physics (MIAPP) of the DFG cluster of excellence 'Origin and Structure of the Universe'. Part of this research was carried out at the Jet Propulsion Laboratory, California Institute of Technology, under a contract with the National Aeronautics and Space Administration.

This study is based on observations made with ESO Telescopes at the La Silla Paranal Observatory under programme IDs 091.D-0764, 092.D-0632 and 096.D-0627 and also based on observations made with the NASA/ESA *Hubble Space Telescope*, obtained from the Data Archive at the Space Telescope Science Institute, which is operated by the Association of Universities for Research in Astronomy, Inc., under NASA contract NAS 5-26555. These observations are associated with programs #13737 and #14166. This research has made use of the NASA/IPAC Infrared Science Archive, which is operated by the Jet Propulsion Laboratory, California Institute of Technology, under contract with the National Aeronautics and Space Administration.

REFERENCES

Alam S. et al., 2015, ApJS, 219, 12
Arnett W. D., 1979, ApJ, 230, L37
Asplund M., Grevesse N., Sauval A. J., Scott P., 2009, ARA&A, 47, 481
Axelrod T. S., 1980, PhD thesis, California University, Santa Cruz
Bloom J. S. et al., 2012, ApJ, 744, L17
Bramich D. M., 2008, MNRAS, 386, L77
Cappellaro E., Mazzali P. A., Benetti S., Danziger I. J., Turatto M., della Valle M., Patat F., 1997, A&A, 328, 203
Cappellaro E. et al., 2001, ApJ, 549, L215
Childress M. J. et al., 2015, MNRAS, 454, 3816
Churazov E. et al., 2014, Nature, 512, 406
Colgate S. A., McKee C., 1969, ApJ, 157, 623
Conley A. et al., 2008, ApJ, 681, 482
Corsi A. et al., 2014, ApJ, 782, 42
Crocker R. M. et al., 2016, preprint (arXiv:1607.03495)
Drozdov D., Leising M. D., Milne P. A., Pearcy J., Riess A. G., Macri L. M., Bryngelson G. L., Garnavich P. M., 2015, ApJ, 805, 71
Fenn D., Plewa T., Gawryszczak A., 2016, MNRAS, 462, 2486
Firth R. E. et al., 2015, MNRAS, 446, 3895
Foley R. J., Kirshner R. P., 2013, ApJ, 769, L1
Fransson C., Jerkstrand A., 2015, ApJ, 814, L2
Fransson C., Kozma C., 1993, ApJ, 408, L25
Graham M. L., Nugent P. E., Sullivan M., Filippenko A. V., Cenko S. B., Silverman J. M., Clubb K. I., Zheng W., 2015, MNRAS, 454, 1948
Graur O., Zurek D., Shara M. M., Riess A. G., Seitenzahl I. R., Rest A., 2016, ApJ, 819, 31
Guy J. et al., 2007, A&A, 466, 11
Hillebrandt W., Niemeyer J. C., 2000, ARA&A, 38, 191
Hillebrandt W., Kromer M., Röpke F. K., Ruiter A. J., 2013, Frontiers Phys., 8, 116
Howell D. A., 2011, Nat. Commun., 2, 350
Hoyle F., Fowler W. A., 1960, ApJ, 132, 565
Hsiao E. Y., Conley A., Howell D. A., Sullivan M., Pritchet C. J., Carlberg R. G., Nugent P. E., Phillips M. M., 2007, ApJ, 663, 1187
Iben I., Jr, Tutukov A. V., 1984, ApJS, 54, 335
Iwamoto K., Brachwitz F., Nomoto K., Kishimoto N., Umeda H., Hix W. R., Thielemann F.-K., 1999, ApJS, 125, 439
Johansson J. et al., 2017, MNRAS, 466, 3442
Kasen D., Nugent P. E., 2013, Annu. Rev. Nucl. Part. Sci., 63, 153
Kerzendorf W. E., Taubenberger S., Seitenzahl I. R., Ruiter A. J., 2014, ApJ, 796, L26
Kozma C., Fransson C., 1998a, ApJ, 496, 946
Kozma C., Fransson C., 1998b, ApJ, 497, 431
Kuchner M. J., Kirshner R. P., Pinto P. A., Leibundgut B., 1994, ApJ, 426, 89
Lair J. C., Leising M. D., Milne P. A., Williams G. G., 2006, AJ, 132, 2024
Law N. M. et al., 2009, PASP, 121, 1395
Leloudas G. et al., 2009, A&A, 505, 265
Li W. et al., 2011, Nature, 480, 348
McClelland C. M., Garnavich P. M., Milne P. A., Shappee B. J., Pogge R. W., 2013, ApJ, 767, 119
Maeda K., Röpke F. K., Fink M., Hillebrandt W., Travaglio C., Thielemann F.-K., 2010, ApJ, 712, 624
Maoz D., Mannucci F., Nelemans G., 2014, ARA&A, 52, 107
Marino S., González-Gaitán S., Förster F., Folatelli G., Hamuy M., Hsiao E., 2015, ApJ, 806, 134
Matheson T. et al., 2012, ApJ, 754, 19
Mazzali P. A. et al., 2014, MNRAS, 439, 1959
Mazzali P. A. et al., 2015, MNRAS, 450, 2631
Milne P. A., The L.-S., Leising M. D., 2001, ApJ, 559, 1019
Munari U., Henden A., Belligoli R., Castellani F., Cherini G., Righetti G. L., Vagnozzi A., 2013, New Astron., 20, 30
Nugent P. E. et al., 2011, Nature, 480, 344
Ofek E. O. et al., 2013, Nature, 494, 65
Ofek E. O. et al., 2014, ApJ, 789, 104
Pakmor R., Kromer M., Taubenberger S., Sim S. A., Röpke F. K., Hillebrandt W., 2012, ApJ, 747, L10
Parrent J. T. et al., 2012, ApJ, 752, L26
Patat F. et al., 2013, A&A, 549, A62
Pereira R. et al., 2013, A&A, 554, A27
Perlmutter S. et al., 1998, Nature, 391, 51

Rahmer G., Smith R., Velur V., Hale D., Law N., Bui K., Petrie H., Dekany R., 2008, Proc. SPIE, 7014, 70144Y
Rau A. et al., 2009, PASP, 121, 1334
Richmond M. W., Smith H. A., 2012, J. Am. Assoc. Var. Star Obser., 40, 872
Riess A. G. et al., 1998, AJ, 116, 1009
Röpke F. K. et al., 2012, ApJ, 750, L19
Schmidt B. P., Kirshner R. P., Leibundgut B., Wells L. A., Porter A. C., Ruiz-Lapuente P., Challis P., Filippenko A. V., 1994, ApJ, 434, L19
Seitenzahl I. R., Taubenberger S., Sim S. A., 2009, MNRAS, 400, 531
Seitenzahl I. R. et al., 2013, MNRAS, 429, 1156
Seitenzahl I. R., Timmes F. X., Magkotsios G., 2014, ApJ, 792, 10
Shappee B. J., Stanek K. Z., 2011, ApJ, 733, 124
Shappee B. J., Stanek K. Z., Pogge R. W., Garnavich P. M., 2013, ApJ, 762, L5
Shappee B. J., Stanek K. Z., Kochanek C. S., Garnavich P. M., 2016, preprint (arXiv:1608.01155)
Siegert T., Diehl R., Vincent A. C., Guglielmetti F., Krause M. G. H., Boehm C., 2016, A&A, 595, A25
Sollerman J. et al., 2004, A&A, 428, 555
Stritzinger M., Sollerman J., 2007, A&A, 470, L1
Strotjohann N. L. et al., 2015, ApJ, 811, 117
Taubenberger S. et al., 2015, MNRAS, 448, L48
Tsvetkov D. Y., Shugarov S. Y., Volkov I. M., Goranskij V. P., Pavlyuk N. N., Katysheva N. A., Barsukova E. A., Valeev A. F., 2013, Contr. Astron. Obser. Skalnate Pleso, 43, 94
Webbink R. F., 1984, ApJ, 277, 355
Whelan J., Iben I., Jr, 1973, ApJ, 186, 1007
Yaron O., Gal-Yam A., 2012, PASP, 124, 668
York D. G. et al., 2000, AJ, 120, 1579
Zhang K. et al., 2016, ApJ, 820, 67

SUPPORTING INFORMATION

Supplementary data are available at *MNRAS* online.

Table A1. PTF photometry for SN 2011fe.

Please note: Oxford University Press is not responsible for the content or functionality of any supporting materials supplied by the authors. Any queries (other than missing material) should be directed to the corresponding author for the article.

APPENDIX A: PHOTOMETRIC DATA

Table A1. PTF photometry for SN 2011fe.

MJD	Phase (d)[a]	Telescope	Filter	Mag (AB)	ΔMag (AB)
56016.138	201.59	P48	*PTF48R*	16.034	0.009
56016.201	201.65	P48	*PTF48R*	16.045	0.016
56016.263	201.72	P48	*PTF48R*	16.058	0.008
56017.170	202.62	P48	*PTF48R*	16.085	0.009
56017.214	202.67	P48	*PTF48R*	16.077	0.009
56017.245	202.70	P48	*PTF48R*	16.073	0.008
56017.463	202.91	P48	*PTF48R*	16.050	0.008
56017.507	202.96	P48	*PTF48R*	16.064	0.008
...	...	...	...	...	...
...	...	...	...	...	...
...	...	...	...	...	...

Note. [a]$\mathrm{MJD_{max}} = 55814.38$, calculated by SiFTO.

This paper has been typeset from a TEX/LATEX file prepared by the author.